







Imaging Se diffusion across the FeSe/SrTiO₃ interface

Samantha O’Sullivan ¹, Ruizhe Kang ², Jules A. Gardener,³ Austin J. Akey ³,
Christian E. Matt ^{1,*} and Jennifer E. Hoffman ^{1,2,†}

¹*Department of Physics, Harvard University, Cambridge, Massachusetts 02138, USA*

²*School of Engineering and Applied Sciences, Harvard University, Cambridge, Massachusetts 02138, USA*

³*Center for Nanoscale Systems, Harvard University, Cambridge, Massachusetts 02138, USA*

 (Received 17 May 2021; revised 25 January 2022; accepted 22 February 2022; published 5 April 2022)

Monolayer FeSe on SrTiO₃ superconducts with reported T_c as high as 100 K, but the dramatic interfacial T_c enhancement remains poorly understood. Oxygen vacancies in SrTiO₃ are known to enhance the interfacial electron doping, electron-phonon coupling, and superconducting gap, but the detailed mechanism is unclear. Here we apply scanning transmission electron microscopy and electron energy loss spectroscopy to FeSe/SrTiO₃ to image the diffusion of selenium into SrTiO₃ to an unexpected depth of several unit cells, consistent with the simultaneously observed depth profile of oxygen vacancies. Our density functional theory calculations support the crucial role of oxygen vacancies in facilitating the thermally driven Se diffusion. In contrast to excess Se in the FeSe *monolayer* or FeSe/SrTiO₃ *interface* that is typically removed during postgrowth annealing, the diffused Se remains in the top few unit cells of the SrTiO₃ *bulk* after the extended postgrowth annealing that is necessary to achieve superconductivity. Thus, the unexpected Se in SrTiO₃ may contribute to the interfacial electron doping and electron-phonon coupling that enhance T_c , suggesting another important role for oxygen vacancies as facilitators of Se diffusion.

DOI: [10.1103/PhysRevB.105.165407](https://doi.org/10.1103/PhysRevB.105.165407)

I. INTRODUCTION

Monolayer FeSe grown on SrTiO₃ (STO) superconducts with a transition temperature T_c as high as 100 K [1–3], an order of magnitude higher than bulk FeSe ($T_c \sim 8.8$ K [4]). While there is general consensus that the interface plays a crucial role in the enhanced superconductivity [5–14], the specific mechanism remains controversial. Angle-resolved photoemission spectroscopy (ARPES), electron energy loss spectroscopy (EELS), and scanning tunneling microscopy (STM) found evidence of a cooperative interplay of two effects: substrate-induced electron doping [6–10] and interfacial electron-phonon coupling [11–15]. But the wide range of measured T_c in nominally similar samples suggests that both effects are strongly influenced by the detailed atomic structure and chemical composition of the interface.

Oxygen plays a key role in both electron doping and electron-phonon coupling at the STO interface. Oxygen vacancies directly donate charge carriers [5–8,16,17] or indirectly alter the STO work function and associated charge transfer induced by band bending [10]. On the other hand, STO surface oxygen and its substitutions control the energy and form of the phonon modes that couple to the FeSe electrons [11,14,15]. Such electron-phonon coupling strongly influences T_c [9,11,12] but could be screened by excess Se at the interface [17]. Finally, the pronounced dependence of electron-phonon coupling on oxygen vacancy

concentration [18,19] complicates the interplay between the electron doping and electron-phonon coupling contributions to T_c . The fact that enhanced superconductivity has been found in monolayer FeSe grown on various oxides, including anatase TiO₂ [20], BaTiO₃ [21], LaTiO₃ [22], NdGaO₃ [23], and MgO [24], but is absent in nonoxide systems [13,25] further emphasizes the importance of oxygen chemistry on FeSe superconductivity.

Selenium belongs to the same chemical family as oxygen, which suggests that Se atoms might fill the O vacancies that typically form during high-temperature vacuum annealing [26–29]. Indeed, such a scenario has been theoretically predicted for oxygen vacancies in the top TiO_{2-x} layer [16] and experimentally supported by ARPES [7] and scanning transmission electron microscopy (STEM) [15,17]. Furthermore, several groups employ high-temperature annealing under high Se pressure to prepare the STO surface prior to FeSe growth [1,30], which might enhance Se diffusion into STO as more oxygen vacancies are created and the formation energy for Se substitution is lowered. Often, excess Se in the FeSe film and at the interface is removed during postgrowth annealing [17], which might not be possible for Se diffused deeper into the STO subsurface. Although accurate knowledge of the interface chemical composition is of profound importance for exact modeling of the superconductivity enhancement in the FeSe/STO heterostructure, no experiment has investigated Se diffusion into subsurface layers of STO.

Here we use STEM and EELS to reveal the diffusion of Se several unit cells deep into STO that occurs during the monolayer FeSe film growth and annealing, both performed at temperatures below ~ 520 °C. We find that the excess Se

*christian.matt87@gmail.com

†jhoffman@physics.harvard.edu

decays exponentially into STO, as predicted by Fick's law of thermally activated elemental diffusion [31]. Furthermore, we observe a similar line profile and decay length of oxygen vacancies at the STO surface which, in combination with density functional theory (DFT) calculations, suggest that oxygen vacancies play a pivotal role in Se diffusion. The role of oxygen vacancies in facilitating Se diffusion is further supported by the contrast between the Se and Fe line profiles and the negligible diffusion of Fe, which belongs to a different chemical family and therefore does not substitute for oxygen.

II. METHODS

Monolayer FeSe was grown by molecular beam epitaxy (MBE) on a Nb-doped (0.05%) STO(001) substrate from Crystek. The STO substrate was etched with buffered HF ($\text{NH}_4\text{F}:\text{HF} = 7:1$, diluted with an equal volume of deionized water) for 30 s, then annealed in O_2 at 950°C for 1 h. The substrate was transferred into the MBE chamber (base pressure $< 5 \times 10^{-10}$ Torr) and degassed for 3 h at 500°C . Importantly, *no* high-temperature Se molecular beam etching was performed prior to growth [1]. FeSe was deposited in three rounds by coevaporating Fe (99.995%) and Se (99.999%) with a molar flux ratio of 1:30 and substrate temperatures between 400°C and 520°C , followed by postgrowth annealing at 450°C – 520°C (first round: 0.95 unit cell FeSe deposited at a substrate temperature of 400°C and 3 h postgrowth annealing at 450°C ; second round: 0.3 unit cell FeSe at 400°C with 3 h postgrowth annealing at 450°C and 4 h at 520°C ; third round: ~ 0.2 unit cell FeSe at 520°C , postgrowth annealed at the same temperature for 4 h). The final annealing step in ultrahigh vacuum (UHV, $< 5 \times 10^{-10}$ Torr) was performed at $\sim 510^\circ\text{C}$ for 10 h. After each growth step the sample was transferred through UHV to a home-built scanning tunneling microscope for imaging at ~ 77 K. The final STM scan confirmed that the high annealing temperature $\gtrsim 500^\circ\text{C}$ was effective in removing all 2 unit cell islands [9]. Finally, the film was capped with an ~ 40 nm Te layer [32] at room temperature to prepare for cross-sectional STEM and EELS measurements. A lamella with a thickness of 30 ± 6 nm was prepared using focused ion beam milling (FEI Helios 660). A JEOL ARM 200F operated at 200 kV was used to record room temperature STEM (JEOL HAADF detector) and EELS measurements at six different locations of the lamella. EELS data was acquired with STEM probe settings of a 197 pA current and a 22.4 mrad convergence angle, using a Gatan Enfinitum EELS spectrometer. We grew a second sample for low-temperature STM imaging and confirmed a superconducting gap of ~ 15 meV at $T = 4.7$ K.

We performed DFT calculations using the open-source QUANTUM ESPRESSO software package [29,33]. We constructed a $3 \times 3 \times 3$ STO supercell, terminated by a double TiO_{2-x} layer, and added 20 Å of vacuum spacing along the (001) axis to simulate the two-dimensional surface structure using periodic boundary conditions. We used ultrasoft pseudopotentials for Sr, Ti, and Se atoms and a projector augmented-wave pseudopotential for O atoms. We set the kinetic energy cutoff to be 40 Ry and the charge density cutoff to 400 Ry. We used a Gaussian smearing of 0.01 Ry to improve

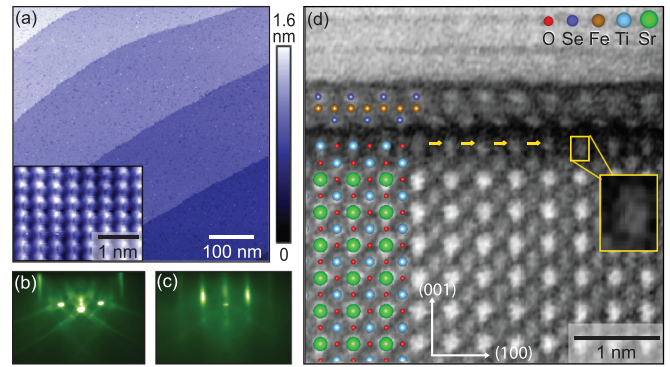


FIG. 1. High-quality monolayer FeSe grown on SrTiO₃ (STO). (a) Topography acquired by STM, with the inset showing the atomically resolved top Se layer (sample bias $V_s = 0.1$ V, current set point $I_s = 90$ pA). (b) and (c) RHEED images of the STO substrate along (100) before and after FeSe film growth (recorded at 15 keV, $T = 400^\circ\text{C}$). (d) Atomic resolution STEM image of monolayer FeSe on the STO substrate with a Te capping layer. Yellow arrows and zoom-in box highlight the elongated shape of the top Ti atoms. FeSe/STO crystal structure is overlaid on the left side of (d).

the convergence during the relaxation. We relaxed the entire structure until both the forces and total energy for ionic minimization were smaller than 1×10^{-4} hartree/bohr and 1×10^{-4} hartree, respectively. The energy convergence threshold for self-consistency was 1×10^{-6} hartree. We sampled the first Brillouin zone by a $4 \times 4 \times 1$ k grid. When relaxing the structure, we allowed only the top three atomic layers (top TiO_{2-x} , second TiO_{2-y} , top SrO) to move, while the rest were fixed.

III. RESULTS

The high crystalline quality of the FeSe film is apparent in the STM topography in Fig. 1(a), showing uniform monolayer coverage and atomically smooth surface areas (see the inset). Reflection high-energy electron diffraction (RHEED) images of the STO surface in Fig. 1(b) show sharp diffraction spots, indicating a nonreconstructed (1×1) termination. The postgrowth RHEED image in Fig. 1(c) depicts the typical pattern for epitaxial monolayer FeSe [2]. Figure 1(d) shows our atomic resolution cross-sectional STEM measurement in which we can identify the Te capping layer, the monolayer FeSe, and an atomically sharp FeSe/STO interface. We measure the interatomic distance between the bottom Se and top Ti layers to be 3.35 ± 0.21 Å, consistent with previous STEM measurement [17]. We also observe the double-layer TiO_{2-x} termination of the STO, which is commonly seen [10,17,34–36]. While we do not observe any ordered Se layer between the FeSe and the top TiO_{2-x} layer [10], we note that the top Ti atoms appear slightly elongated along the (001) direction, which has been interpreted as a sign of additional Se at the interface [17].

To identify the chemical composition of the interface, we analyze the EELS measurement over a wide energy range covering Ti, Fe, Se, O, and Sr absorption edges. We average the absorption spectra along the (100) direction of the scan window and subtract a power law background, as

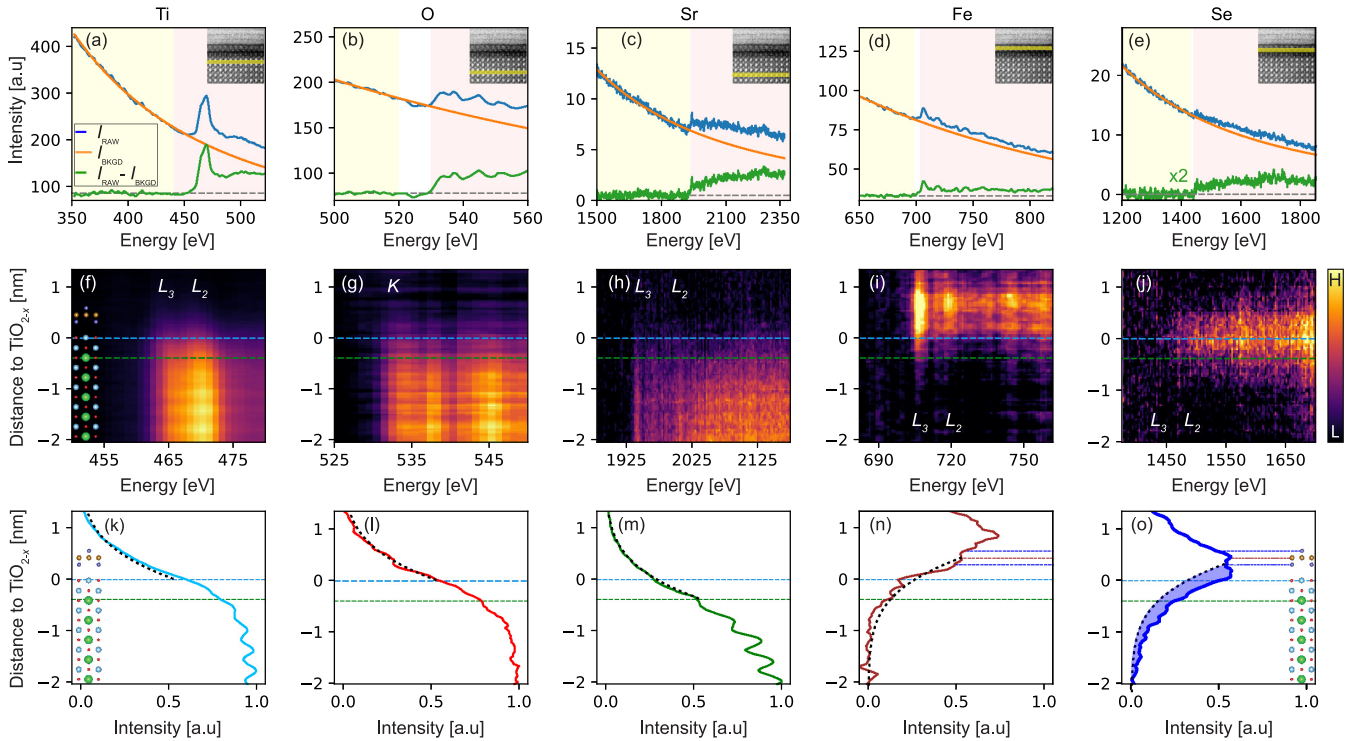


FIG. 2. (a)–(e) EELS signals and the background subtraction process for elements Ti, O, Sr, Fe, and Se. The background fitting range is shaded yellow, and the signal integration range is shaded pink, with the raw signal intensity I_{RAW} (averaged along the yellow line in the corresponding inset) in blue, the fit background intensity I_{BKGD} in orange, and the difference of the two ($I_{\text{RAW}} - I_{\text{BKGD}}$) in green. Arbitrary vertical offset (gray dashed line) has been added to each ($I_{\text{RAW}} - I_{\text{BKGD}}$) curve for visual purposes. (f)–(j) Energy loss with single measurement region, averaged along the (100) direction at indicated absorption edges after background subtraction ($I_{\text{RAW}} - I_{\text{BKGD}}$), with the color bar denoting low (L) to high (H) intensity. Dashed blue (green) lines indicate positions of the upper TiO_{2-x} (SrO) layers. (k)–(o) Energy-integrated linecuts of energy loss plots averaged over six measurement regions. Maximum intensities of Ti, O, and Sr are normalized to 1. Fe and Se are normalized to the expected intensity of a single layer using the resolution broadening (black dotted line) inferred from the Sr edge (see Fig. 6). The resolution-broadened beam profile is shown in each panel as an identical black dotted curve, shifted or reflected appropriately.

shown in Figs. 2(a)–2(e) (see also Appendix A and Fig. 5). Figures 2(f)–2(j) show a resolution-limited cutoff for Ti, O, and Sr above the top TiO_{2-x} layer and for Fe below the TiO_{2-x} layer, as expected for an atomically sharp interface. In contrast, we find that the Se intensity has a longer tail below the top TiO_{2-x} layer shown in Fig. 2(j), suggesting that Se diffused into the STO substrate. This observation is confirmed in the energy-integrated linecuts, shown in Figs. 2(k)–2(o). The intensity drops of Ti, O above the topmost TiO_{2-x} layer, and Sr above the SrO layer are determined by the beam shape of the STEM probe (see Appendix B and Fig. 6). The Fe linecut follows the same expected resolution-limited intensity profile, dropping just above the TiO_{2-x} line. However, the Se linecut deviates significantly from the expected profile and extends at higher intensities for several STO subsurface layers, indicating a significant concentration of Se below the top TiO_{2-x} layer.

The contrast between Se and Fe *downward* diffusion is shown by the differing deviations of their measured linecuts from their expected resolution-broadened intensity profiles in Figs. 2(n) and 2(o). While the excess Fe signal below the Fe layer in Fig. 2(n) is within the instrument broadening and noise level, the excess Se, marked by the blue shaded area in Fig. 2(o), is significant and extends deep into the subsurface

layer of STO. The Fe intensity peak *above* the FeSe monolayer may indicate the presence of excess Fe that formed FeTe islands during the Te capping process, as previously suggested by Refs. [37,38].

To investigate the origin of Se diffusion into STO and a possible connection with preformed O vacancies, we analyze their spatial profile across the interface in Fig. 3. The excess Se signal peaks just above the TiO_{2-x} layer and falls exponentially along the (00 $\bar{1}$) direction with decay length $\xi_{\text{Se}} = 0.74 \pm 0.05$ nm (vertical black arrow). The peak position above the TiO_{2-x} layer demonstrates excess Se between STO and the FeSe layer, consistent with Fig. 1(d) and previous STEM studies [10,17]. The exponential profile is a solution of Fick’s diffusion law [31], which points towards thermally driven diffusion along an element concentration gradient, as is often observed at interfaces [39]. However, the contrasting absence of Fe diffusion into the STO suggests that thermal activation alone is not sufficient, and a second mechanism must contribute to the Se diffusion into the STO substrate. Selenium belongs to the same chemical family as oxygen, suggesting that oxygen vacancies may be partially filled with Se, similar to predictions for the top TiO_{2-x} layer [16,17]. Figure 3 shows the concentration of O vacancies extracted from the spatial dependence of the O_2/Ti ratio of the EELS

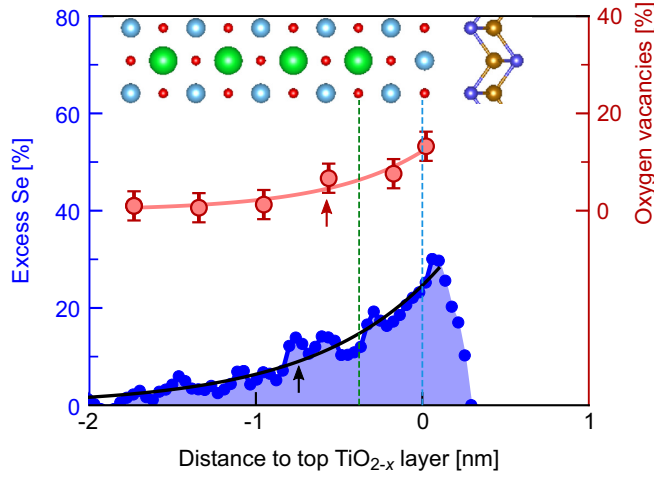


FIG. 3. Excess selenium at the substrate surface correlates with oxygen vacancy formation. Left axis: Excess selenium (as a fraction of the lower Se layer in FeSe) calculated by subtracting the dotted black line from the Se signal in Fig. 2(o). Right axis: Increasing formation of oxygen vacancies towards the STO surface extracted from the O_2/Ti ratio of linecuts in Figs. 2(k) and 2(l). Vertical arrows indicate decay length.

linecuts in Figs. 2(k) and 2(l). We find an exponential decay length of $\xi_{O_{vac}} = 0.57 \pm 0.30$ nm (red arrow), corresponding to an O vacancy concentration of $11\% \pm 3\%$ for the top TiO_{2-x} layer and $6\% \pm 3\%$ for the second TiO_{2-y} layer. The consistency between ξ_{Se} and $\xi_{O_{vac}}$ supports the hypothesis that oxygen vacancies are crucial in facilitating the Se diffusion into STO.

To further investigate the role of oxygen vacancies on Se diffusing into the STO surface, we use DFT to calculate the formation energies for various vacancy configurations (for more details, see Sec. II and Appendix C). In our calculations we assume that oxygen vacancies form during vacuum annealing prior to FeSe growth. We investigate the following two configurations: (i) one vacancy per supercell in the top TiO_{2-x} layer, corresponding to 5.5% O vacancies, and (ii) two vacancies (11%) in the top TiO_{2-x} layer and one vacancy (5.5%) in the second TiO_{2-y} layer, corresponding to the measured number of oxygen vacancies in Fig. 3 (see Appendix C and Fig. 7). Figures 4(a)–4(d) show the final relaxed structures after we filled each oxygen vacancy with Se (Se_O). Our calculation shows that Se_O in the top TiO_{2-x} layer protrudes slightly from the layer, consistent with our experimental observation of apparent Ti atom elongation in Fig. 1(d) and the excess Se peak just above the TiO_{2-x} layer in Fig. 3. In contrast, the Se_O in the second TiO_{2-y} layer remains at its initial location, suggesting that diffused Se predominantly occupies the oxygen vacancy sites instead of interstitial locations. We next calculate the formation energies for Se atoms filling the vacancies,

$$E_{form} = E_{nSe}^{DFT} - E_{nO_{vac}}^{DFT} - n\mu_{Se}. \quad (1)$$

Here $E_{nO_{vac}}^{DFT}$ and E_{nSe}^{DFT} are the energies of the fully relaxed structure with n oxygen vacancies and n Se substitutions, respectively, and μ_{Se} is the temperature- and pressure-dependent chemical potential of a single Se atom. In Fig. 4(e),

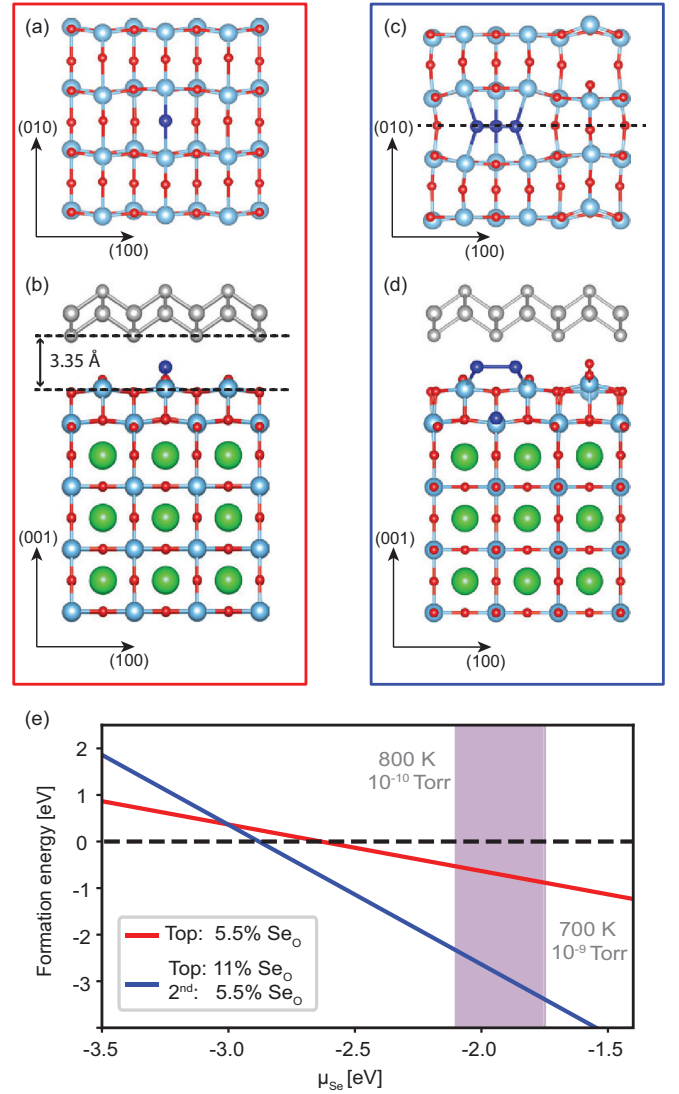


FIG. 4. (a) Top view and (b) side view of the fully relaxed structure, where a single Se atom (dark blue sphere) substitutes one oxygen vacancy on the top TiO_{2-x} layer, corresponding to 5.5% Se_O substitution. (c) and (d) Same as (a) and (b), but with three Se atoms substituting two oxygen vacancies (11% Se_O) in the top TiO_{2-x} layer and one oxygen vacancy (5.5% Se_O) in the second TiO_{2-y} layer, at indicated locations. Note that only the top two layers of atoms are shown in (a) and (c). The FeSe layers in (b) and (d) are shown in gray as a guide to the eye and are not included in the DFT calculation. (e) Formation energy as a function of the Se chemical potential. The purple region indicates realistic experimental conditions with substrate temperatures and Se partial pressures as indicated.

we find that E_{form} is negative for a range of μ_{Se} corresponding to experimental substrate temperatures and Se partial pressures, marked by the purple shaded area (see Appendixes C and D). Our calculations thus suggest that Se diffusion below the top TiO_{2-x} layer is energetically favorable in the presence of oxygen vacancies.

We consider the implications of Se diffusion for the charge carrier concentration in STO. While O vacancies create free electrons at the STO surface, which likely dope the monolayer FeSe [5,7], excess Se has been theoretically [40,41] and

experimentally [5,7] shown to act as a hole dopant. However, as the electronegativity of Se (2.55) is lower than that of O (3.44), we expect that even in the extreme case of all O vacancies being filled with Se, excess free electrons will remain. Furthermore, the excess Se could influence the STO work function and the associated interfacial band bending, altering the electron transfer into FeSe [10]. The STO charge carrier concentration also modifies the electron-phonon coupling [18,19]. Additional theoretical and experimental study is required to understand the detailed effects of subsurface Se on the interfacial electron-phonon coupling, charge transfer, and superconductivity enhancement.

IV. CONCLUSION

To conclude, we imaged the monolayer FeSe/STO interface using atomic resolution STEM and EELS, and we observed Se diffusion several unit cells deep into the STO. Our EELS measurements further revealed oxygen vacancies in the surface and subsurface layers of STO, which, in combination with our DFT calculations, supports the scenario that oxygen vacancies are crucial to facilitate Se diffusion. Surprisingly, the diffused Se persisted in the STO even after extended (~ 10 h) postgrowth UHV annealing above 500°C , which has been shown to remove excess Se from the FeSe layer and the immediate interface between FeSe and STO [17]. The postgrowth annealing is a crucial step to obtain the high-temperature superconductivity in the FeSe/STO heterostructure [7,17]. Our findings call for future experiments to measure the relation between Se diffusion depth and superconducting T_c and future theoretical models to calculate the effects of Se diffusion on electron-phonon coupling and interfacial doping. Our observation may also help to resolve the inconsistency between the calculated [42] and experimentally measured band structure of the monolayer FeSe/STO heterostructure [6,11].

ACKNOWLEDGMENTS

We thank Yu Xie, Boris Kozinsky, Dennis Huang, and Jason Hoffman for insightful discussions. This work was performed in part at the Center for Nanoscale Systems (CNS), a member of the National Nanotechnology Coordinated Infrastructure Network (NNCI), which is supported by the National Science Foundation under Award No. ECCS-2025158. CNS is part of Harvard University. C.E.M. was supported by the Swiss National Science Foundation under Fellowships No. P2EZF2_175155 and No. P400P2_183890 and by Office of Naval Research Grant No. N00014-18-1-2691.

APPENDIX A: SELENIUM ABSORPTION EDGE

Figure 5 shows the evolution of the Se absorption spectra across the FeSe/STO interface within one representative region. The location of the lower Se layer is marked by a blue line in all three panels. The Se L edge after background subtraction is shown in false color in Fig. 5(b) and as a line-cut in Fig. 5(c). The total Se signal for each position along the (001) direction is the integrated green area under each curve. We reproduced these data in six distinct regions along

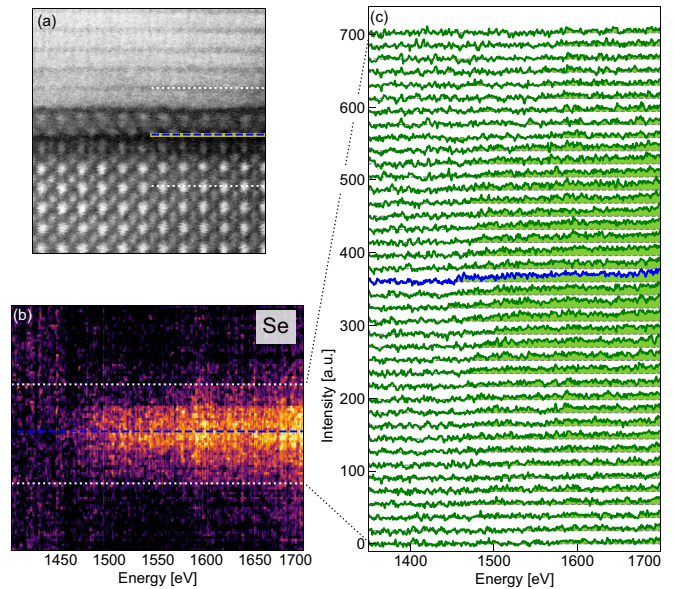


FIG. 5. Spatial evolution of the Se absorption edge. (a) High-resolution STEM image as shown in Fig. 1(d). (b) Background-subtracted energy loss spectra close to the Se L absorption edge, averaged along the (100) direction of (a), as shown in Fig. 2(j). (c) Line plots of background-subtracted Se energy loss spectra for the (001) range between the white dotted lines in (a) and (b). Blue lines in all three panels indicate the position of the lower Se layer, where the spectrum presented in Fig. 2(e) was extracted.

the FeSe/STO lamella, and we show the averaged results in Fig. 2(o).

APPENDIX B: STEM SPATIAL RESOLUTION

To determine spatial broadening due to the finite STEM electron beam width, we fit Gaussian curves to the tails of the Ti and Sr EELS signals that extend above the top Ti and Sr layers in Figs. 2(k) and 2(m). In Fig. 6, we show

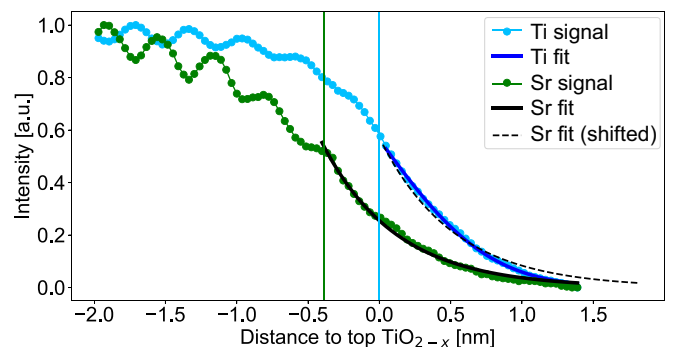


FIG. 6. Instrumental resolution. Tails of titanium (blue) and strontium (green) line shapes from Figs. 2(k) and 2(m) fit by a Gaussian curve (solid lines) above the top Ti and Sr layers in STO, respectively. The locations of the top Ti and Sr layers are indicated by blue and green vertical lines, respectively. We assume a stoichiometric Sr layer and no Sr above; thus, the Sr fit (black solid line) determines the broadening of the STEM signal due to the finite width of the electron beam.

both signals and fits, and we also shift the Sr fit to overlap with the Ti fit, which demonstrates a similar line shape (Sr is slightly broader). The similarity indicates a spatial resolution that is almost independent of energy (absorption energies: Ti L_3 edge, 456 eV; Sr L_3 edge, 1940 eV). We then compare the Sr fit tail (representing pure instrument broadening) to our Fe and Se line profiles in Figs. 2(n) and 2(o) to determine the Fe and Se excess signal that corresponds to real element diffusion into the STO bulk. Since the monolayer FeSe consists of only one Fe layer and two Se layers, we expect the peak amplitude of these element profiles to be reduced due to the finite spatial resolution. We therefore normalize the Fe and Se profiles in Figs. 2(n) and 2(o) such that the intensity of the Fe (Se) profile at the location of the Fe (Se) layer equals the Sr signal at the top Sr layer (which is less than the Sr signal in the bulk of STO).

APPENDIX C: FORMATION ENERGY OF SELENIUM DIFFUSION

Electrical [27], magnetic resonance [28,29], and optical [26] studies have shown that oxygen vacancies occur during heat treatment in vacuum near the surface of STO substrates. Thus, our DFT calculations start from supercell models that have oxygen vacancies on the top two layers of TiO_{2-x} . We define the formation energy using

$$E_{\text{form}} = E_{n\text{Se}}^{\text{DFT}} - E_{n\text{O}_{\text{vac}}}^{\text{DFT}} - n\mu_{\text{Se}}, \quad (\text{C1})$$

where $E_{n\text{Se}}^{\text{DFT}}$ is the energy of the fully relaxed structure with Se implemented in either the top or the second TiO_{2-x} layer. $E_{n\text{O}_{\text{vac}}}^{\text{DFT}}$ is the energy of the fully relaxed STO supercell with vacancies in either the top or the second TiO_{2-x} layer. Both of them are calculated by DFT. μ_{Se} is the chemical potential of a single Se atom, which is a function of temperature T and pressure p . μ_{Se} can be written as

$$\mu_{\text{Se}}(T, p) = \frac{1}{2}\mu_{\text{Se}_2} = \frac{1}{2}[E_{\text{Se}_2}^{\text{DFT}} + \mu_{\text{Se}_2}(T, p)], \quad (\text{C2})$$

where $E_{\text{Se}_2}^{\text{DFT}}$ is the energy of an isolated Se dimer molecule as calculated by DFT. Since it is well known that DFT tends to overbind the molecule [43], we then use Eq. (C3) to finally determine the energy of the Se_2 molecule,

$$E_{\text{Se}_2}^{\text{DFT}} = 2E_{\text{Se}}^{\text{DFT}} - E_{\text{bond}}, \quad (\text{C3})$$

where $E_{\text{Se}}^{\text{DFT}}$ is the energy of an isolated single Se atom determined by a self-consistent DFT calculation. E_{bond} is the bond energy of the Se_2 molecules obtained from Ref. [44], and $\mu_{\text{Se}_2}(T, p)$ in Eq. (C2) is the chemical potential for the selenium dimer molecule, which depends on temperature and pressure, as derived in Appendix D.

To calculate the formation energy, we first fully relaxed the pristine STO supercell with a double-layer TiO_{2-x} termination. The calculated distance between the double TiO_{2-x} layers is 2.19 Å, which is very close to our experimental value of $\sim 1.9 \pm 0.3$ Å and confirms the validity of our relaxed structure. We then calculated various oxygen vacancy configurations and their relaxed crystal structures and energies $E_{n\text{O}_{\text{vac}}}^{\text{DFT}}$ for each case. Consecutively, we replaced each

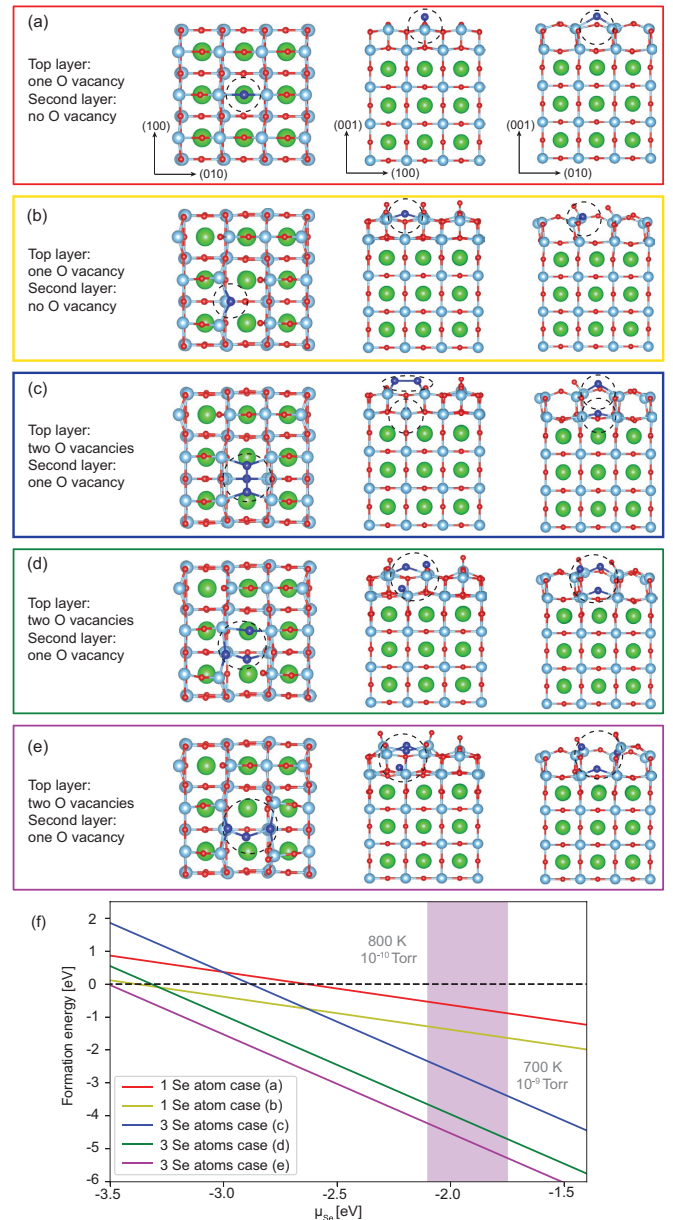


FIG. 7. Relaxed crystal structures and formation energy of Se-substituted oxygen vacancies. (a)–(e) Relaxed $3 \times 3 \times 3$ supercell with (a) and (b) one oxygen vacancy replaced by SeO in the top TiO_{2-x} layer ($2x \sim 5.5\%$) and (c)–(e) three oxygen vacancies replaced by SeO , two in the top TiO_{2-x} layer ($2x = 11\%$) and one in the second TiO_{2-y} layer ($2y = 5.5\%$), calculated for three different configurations. In each case, Se in the top TiO_{2-x} layer slightly protrudes out of plane, giving rise to the vertically elongated Ti appearance in the STEM images in Fig. 1(d) and reported in Ref. [17]. (f) Formation energies for the cases in (a)–(e), calculated using Eq. (C1), demonstrating that it is favorable (lowers the energy) for the system to fill in preformed oxygen vacancies with Se atoms under realistic experimental conditions of Se partial pressure and sample temperature (purple shaded area).

oxygen vacancy with a selenium atom and again relaxed the supercell to obtain $E_{n\text{Se}}^{\text{DFT}}$ and the final structures presented in Figs. 4(a)–4(d) and 7.

APPENDIX D: ESTIMATION OF THE CHEMICAL POTENTIAL OF A SINGLE SELENIUM ATOM

To estimate the chemical potential of a single Se atom, we determine the chemical potential for a selenium dimer molecule. Considering the Se_2 molecule as an ideal diatomic gas, its partition function has contributions from translation, vibration, and rotation, which can be written as

$$Z = Z_{\text{trans}} Z_{\text{vib}} Z_{\text{rot}}. \quad (\text{D1})$$

Here we ignore the contribution from the electronic levels since they will contribute to the thermodynamic properties only at high temperature or if unpaired electrons are present [45].

Using the rigid rotor-harmonic oscillator approximation [45,46], one can explicitly evaluate all the thermodynamic quantities. The chemical potential can be expressed in terms of a reference pressure as shown in [47],

$$\mu_{\text{Se}_2}(T, p) = \mu_{\text{Se}_2}^0(T, p^0) + k_B T \log\left(\frac{p}{p^0}\right), \quad (\text{D2})$$

where $\mu_{\text{Se}_2}^0$ is the chemical potential at reference pressure p^0 , which is usually taken to be 1 atm, and k_B is the Boltzmann constant.

Table I shows some of the calculated values of thermodynamical quantities within the temperature range that is close to our experimental condition. The enthalpy H and entropy S were adapted from Ref. [45], and the chemical potential $\mu_{\text{Se}_2}^0$

TABLE I. Calculated thermodynamical properties of a selenium molecule at 1 atm.

| T (K) | H (kJ/mol) [45] | S (J/mol/K) [45] | $\mu_{\text{Se}_2}^0$ (eV) |
|---------|-------------------|--------------------|----------------------------|
| 500 | 14.53 | 270.86 | -1.25 |
| 600 | 17.46 | 277.57 | -1.54 |
| 700 | 20.40 | 283.27 | -1.84 |
| 800 | 23.34 | 288.23 | -2.15 |
| 900 | 26.29 | 292.61 | -2.46 |

is defined as the Gibbs free energy G per molecule,

$$\mu_{\text{Se}_2}^0 = \frac{G}{N_A} = \frac{H - TS}{N_A}. \quad (\text{D3})$$

If we insert the values from Table I into Eq. (D2), we will obtain the chemical potential for a single Se_2 molecule at any given temperature and pressure. Given our experimental conditions, here we consider two extreme cases:

(i) For $T = 800$ K and pressure $p = 10^{-10}$ Torr, $\mu_{\text{Se}_2} = -4.20$ eV, which is the lower limit.

(ii) For $T = 700$ K and pressure $p = 10^{-9}$ Torr, $\mu_{\text{Se}_2} = -3.50$ eV, which is the upper limit.

Plugging these values into Eq. (C2), we can estimate that under our experimental conditions, the range of the chemical potential for a single Se atom (for simplicity, here we set $E_{\text{Se}}^{\text{DFT}} = 0$) is

$$\mu_{\text{Se}}(T, p) \in [-2.10 \text{ eV}, -1.75 \text{ eV}]. \quad (\text{D4})$$

- [1] Q.-Y. Wang, Z. Li, W.-H. Zhang, Z.-C. Zhang, J.-S. Zhang, W. Li, H. Ding, Y.-B. Ou, P. Deng, K. Chang, J. Wen, C.-L. Song, K. He, J.-F. Jia, S.-H. Ji, Y.-Y. Wang, L.-L. Wang, X. Chen, X.-C. Ma, and Q.-K. Xue, Interface-induced high-temperature superconductivity in single unit-cell FeSe films on SrTiO_3 , *Chin. Phys. Lett.* **29**, 037402 (2012).
- [2] D. Huang and J. E. Hoffman, Monolayer FeSe on SrTiO_3 , *Annu. Rev. Condens. Matter Phys.* **8**, 311 (2017).
- [3] J.-F. Ge, Z.-L. Liu, C. Liu, C.-L. Gao, D. Qian, Q.-K. Xue, Y. Liu, and J.-F. Jia, Superconductivity above 100 K in single-layer FeSe films on doped SrTiO_3 , *Nat. Mater.* **14**, 285 (2015).
- [4] A. E. Böhmer, V. Taufour, W. E. Straszheim, T. Wolf, and P. C. Canfield, Variation of transition temperatures and residual resistivity ratio in vapor-grown FeSe, *Phys. Rev. B* **94**, 024526 (2016).
- [5] W. Zhang, Z. Li, F. Li, H. Zhang, J. Peng, C. Tang, Q. Wang, K. He, X. Chen, L. Wang, X. Ma, and Q.-K. Xue, Interface charge doping effects on superconductivity of single-unit-cell FeSe films on SrTiO_3 substrates, *Phys. Rev. B* **89**, 060506(R) (2014).
- [6] D. Liu *et al.*, Electronic origin of high-temperature superconductivity in single-layer FeSe superconductor, *Nat. Commun.* **3**, 931 (2012).
- [7] S. He *et al.*, Phase diagram and electronic indication of high-temperature superconductivity at 65 K in single-layer FeSe films, *Nat. Mater.* **12**, 605 (2013).
- [8] S. Tan, Y. Zhang, M. Xia, Z. Ye, F. Chen, X. Xie, R. Peng, D. Xu, Q. Fan, H. Xu, J. Jiang, T. Zhang, X. Lai, T. Xiang, J. Hu, B. Xie, and D. Feng, Interface-induced superconductivity and strain-dependent spin density waves in FeSe/ SrTiO_3 thin films, *Nat. Mater.* **12**, 634 (2013).
- [9] H. Zhang, D. Zhang, X. Lu, C. Liu, G. Zhou, X. Ma, L. Wang, P. Jiang, Q.-K. Xue, and X. Bao, Origin of charge transfer and enhanced electron-phonon coupling in single unit-cell FeSe films on SrTiO_3 , *Nat. Commun.* **8**, 214 (2017).
- [10] W. Zhao, M. Li, C.-Z. Chang, J. Jiang, L. Wu, C. Liu, J. S. Moodera, Y. Zhu, and M. H. W. Chan, Direct imaging of electron transfer and its influence on superconducting pairing at FeSe/ SrTiO_3 interface, *Sci. Adv.* **4**, eaao2682 (2018).
- [11] J. J. Lee, F. T. Schmitt, R. G. Moore, S. Johnston, Y.-T. Cui, W. Li, M. Yi, Z. K. Liu, M. Hashimoto, Y. Zhang, D. H. Lu, T. P. Devereaux, D.-H. Lee, and Z.-X. Shen, Interfacial mode coupling as the origin of the enhancement of T_c in FeSe films on SrTiO_3 , *Nature (London)* **515**, 245 (2014).
- [12] Q. Song, T. L. Yu, X. Lou, B. P. Xie, H. C. Xu, C. H. P. Wen, Q. Yao, S. Y. Zhang, X. T. Zhu, J. D. Guo, R. Peng, and D. L. Feng, Evidence of cooperative effect on the enhanced superconducting transition temperature at the FeSe/ SrTiO_3 interface, *Nat. Commun.* **10**, 758 (2019).
- [13] W. H. Zhang, X. Liu, C. H. P. Wen, R. Peng, S. Y. Tan, B. P. Xie, T. Zhang, and D. L. Feng, Effects of surface electron doping and substrate on the superconductivity of epitaxial FeSe films, *Nano Lett.* **16**, 1969 (2016).
- [14] S. Zhang, J. Guan, X. Jia, B. Liu, W. Wang, F. Li, L. Wang, X. Ma, Q. Xue, J. Zhang, E. W. Plummer, X. Zhu, and J. Guo, Role of SrTiO_3 phonon penetrating into thin FeSe films in the

- enhancement of superconductivity, *Phys. Rev. B* **94**, 081116(R) (2016).
- [15] G. Gong, H. Yang, Q. Zhang, C. Ding, J. Zhou, Y. Chen, F. Meng, Z. Zhang, W. Dong, F. Zheng, P. Zhang, L. Yang, L. Gu, Q.-K. Xue, and L. Wang, Oxygen vacancy modulated superconductivity in monolayer FeSe on SrTiO_{3-δ}, *Phys. Rev. B* **100**, 224504 (2019).
- [16] J. Bang, Z. Li, Y. Y. Sun, A. Samanta, Y. Y. Zhang, W. Zhang, L. Wang, X. Chen, X. Ma, Q.-K. Xue, and S. B. Zhang, Atomic and electronic structures of single-layer FeSe on SrTiO₃(001): The role of oxygen deficiency, *Phys. Rev. B* **87**, 220503(R) (2013).
- [17] F. Li, Q. Zhang, C. Tang, C. Liu, J. Shi, C. Nie, G. Zhou, Z. Li, W. Zhang, C.-L. Song, K. He, S. Ji, S. Zhang, L. Gu, L. Wang, X.-C. Ma, and Q.-K. Xue, Atomically resolved FeSe/SrTiO₃(001) interface structure by scanning transmission electron microscopy, *2D Mater.* **3**, 024002 (2016).
- [18] C. Chen, J. Avila, E. Frantzeskakis, A. Levy, and M. C. Asensio, Observation of a two-dimensional liquid of fröhlich polarons at the bare SrTiO₃ Surface, *Nat. Commun.* **6**, 8585 (2015).
- [19] Z. Wang *et al.*, Tailoring the nature and strength of electron-Phonon interactions in the SrTiO₃(001) 2D electron liquid, *Nat. Mater.* **15**, 835 (2016).
- [20] H. Ding, Y.-F. Lv, K. Zhao, W.-L. Wang, L. Wang, C.-L. Song, X. Chen, X.-C. Ma, and Q.-K. Xue, High-Temperature Superconductivity in Single-Unit-Cell FeSe Films on Anatase TiO₂, *Phys. Rev. Lett.* **117**, 067001 (2016).
- [21] R. Peng, H. C. Xu, S. Y. Tan, H. Y. Cao, M. Xia, X. P. Shen, Z. C. Huang, C. H. P. Wen, Q. Song, T. Zhang, B. P. Xie, X. G. Gong, and D. L. Feng, Tuning the band structure and superconductivity in single-layer FeSe by interface engineering, *Nat. Commun.* **5**, 5044 (2014).
- [22] T. Jia, Z. Chen, S. N. Rebec, M. Hashimoto, D. Lu, T. P. Devereaux, D.-H. Lee, R. G. Moore, and Z.-X. Shen, Magic doping and robust superconductivity in monolayer FeSe on titanates, *Adv. Sci.* **8**, 2003454 (2021).
- [23] H. Yang, G. Zhou, Y. Zhu, G.-M. Gong, Q. Zhang, M. Liao, Z. Li, C. Ding, F. Meng, M. Rafique, H. Wang, L. Gu, D. Zhang, L. Wang, and Q.-K. Xue, Superconductivity above 28 K in single unit cell FeSe films interfaced with GaO_{2-δ} layer on NdGaO₃(110), *Sci. Bull.* **64**, 490 (2019).
- [24] G. Zhou, Q. Zhang, F. Zheng, D. Zhang, C. Liu, X. Wang, C.-L. Song, K. He, X.-C. Ma, L. Gu, P. Zhang, L. Wang, and Q.-K. Xue, Interface enhanced superconductivity in monolayer FeSe films on MgO(001): Charge transfer with atomic substitution, *Sci. Bull.* **63**, 747 (2018).
- [25] C.-L. Song, Y.-L. Wang, Y.-P. Jiang, Z. Li, L. Wang, K. He, X. Chen, X.-C. Ma, and Q.-K. Xue, Molecular-beam epitaxy and robust superconductivity of stoichiometric FeSe crystalline films on bilayer graphene, *Phys. Rev. B* **84**, 020503(R) (2011).
- [26] D. A. Tenne, I. E. Gonenli, A. Soukiassian, D. G. Schlom, S. M. Nakhmanson, K. M. Rabe, and X. X. Xi, Raman study of oxygen reduced and re-oxidized strontium titanate, *Phys. Rev. B* **76**, 024303 (2007).
- [27] K. Szot, W. Speier, R. Carius, U. Zastrow, and W. Beyer, Localized Metallic Conductivity and Self-Healing During Thermal Reduction of SrTiO₃, *Phys. Rev. Lett.* **88**, 075508 (2002).
- [28] R. Merkle and J. Maier, Defect association in acceptor-doped SrTiO₃: Case study for Fe_{Ti}V_O[•] and Mn_{Ti}V_O[•], *Phys. Chem. Chem. Phys.* **5**, 2297 (2003).
- [29] M. E. Zvanut, S. Jeddy, E. Towett, G. M. Janowski, C. Brooks, and D. Schlom, An annealing study of an oxygen vacancy related defect in SrTiO₃ substrates, *J. Appl. Phys.* **104**, 064122 (2008).
- [30] M. Xu, X. Song, and H. Wang, Substrate and band bending effects on monolayer FeSe on SrTiO₃(001), *Phys. Chem. Chem. Phys.* **19**, 7964 (2017).
- [31] *Springer Handbook of Electronic and Photonic Materials*, edited by S. Kasap and P. Capper (Springer, Cham, 2017).
- [32] Y. Li, Z. Wang, R. Xiao, Q. Li, K. Wang, A. Richardella, J. Wang, and N. Samarth, Capping layer influence and isotropic in-plane upper critical field of the superconductivity at the FeSe/SrTiO₃ interface, *Phys. Rev. Mater.* **5**, 034802 (2021).
- [33] F. V. E. Hensling, C. Xu, F. Gunkel, and R. Dittmann, Unraveling the enhanced oxygen vacancy formation in complex oxides during annealing and growth, *Sci. Rep.* **7**, 39953 (2017).
- [34] N. Erdman, K. R. Poeppelmeier, M. Asta, O. Warschkow, D. E. Ellis, and L. D. Marks, The structure and chemistry of the TiO₂-rich surface of SrTiO₃(001), *Nature (London)* **419**, 55 (2002).
- [35] G.-Z. Zhu, G. Radtke, and G. A. Botton, Bonding and structure of a reconstructed (001) surface of SrTiO₃ from TEM, *Nature (London)* **490**, 384 (2012).
- [36] M. S. J. Marshall, A. E. Becerra-Toledo, L. D. Marks, and M. R. Castell, Defects on strontium titanate, in *Defects at Oxide Surfaces*, edited by J. Jupille and G. Thornton, Springer Series in Surface Sciences (Springer, Cham, 2015), pp. 327–349.
- [37] Y. Hu, Y. Xu, Q. Wang, L. Zhao, S. He, J. Huang, C. Li, G. Liu, and X. J. Zhou, Identification of a large amount of excess Fe in superconducting single-layer FeSe/SrTiO₃ films, *Phys. Rev. B* **97**, 224512 (2018).
- [38] Y. Hu *et al.*, Discovery of an insulating parent phase in single-layer FeSe/SrTiO₃ films, *Phys. Rev. B* **102**, 115144 (2020).
- [39] H. C. Casey and G. L. Pearson, Diffusion in Semiconductors, in *Point Defects in Solids*, Vol. 2, *Semiconductors and Molecular Crystals*, edited by J. H. Crawford and L. M. Slifkin (Springer, Boston, 1975), pp. 163–255.
- [40] T. Berlijn, H.-P. Cheng, P. J. Hirschfeld, and W. Ku, Doping effects of Se vacancies in monolayer FeSe, *Phys. Rev. B* **89**, 020501(R) (2014).
- [41] K. V. Shanavas and D. J. Singh, Doping SrTiO₃ supported FeSe by excess atoms and oxygen vacancies, *Phys. Rev. B* **92**, 035144 (2015).
- [42] L. V. Tikhonova and M. M. Korshunov, Effect of the additional Se layer on the electronic structure of iron-based superconductor FeSe/SrTiO₃, *J. Supercond. Novel Magn.* **33**, 171 (2020).
- [43] A. Lindman, P. Erhart, and G. Wahnström, Implications of the band gap problem on oxidation and hydration in acceptor-doped barium zirconate, *Phys. Rev. B* **91**, 245114 (2015).
- [44] *Inorganic Chemistry: Principles of Structure and Reactivity*, 4th ed., edited by J. E. Huheey, E. A. Keiter, and R. L. Keiter (Harper Collins, New York, NY, 1993), p. A32.
- [45] S. Tiwari, P. Tandon, and K. N. Uttam, Thermodynamical quantities of chalcogenide dimers (O₂, S₂, Se₂, and Te₂) from spectroscopic data, *J. Spectroscopy* **2013**, 956581 (2012).
- [46] D. A. McQuarrie, *Statistical Mechanics* (Harper & Row, New York, 1976).
- [47] U. Otgonbaatar, W. Ma, M. Youssef, and B. Yildiz, Effect of niobium on the defect chemistry and oxidation kinetics of tetragonal ZrO₂, *J. Phys. Chem. C* **118**, 20122 (2014).